Unsteady Lift Generation on a Low-Aspect-Ratio, Rotating Flat Plate

B.A. Needleman[1], J.R. Harvey[2], M. Jones[2], J. Soria[1], J.L. Palmer[2]

[1]Department of Mechanical and Aerospace Engineering
Monash University, Clayton, Victoria, 3800, Australia

[2]Aerospace Division
Defence Science and Technology Organisation, Fishermans Bend, Victoria, 3207, Australia

Abstract

Experiments have been conducted to measure the transient lift on a flat plate with an aspect ratio of one undergoing rotation in quiescent air. The plate (or wing) smoothly accelerates from rest to a constant angular velocity. The geometry and rotational motion of the wing match those used in computational fluid dynamics simulations by Garmann *et al.*, *Phys. Fluids* **25**(3). The chord-based Reynolds number, defined at the mid-span of the wing, varies from 7600 to 31 000.

The experimental results show good agreement with the computational prediction of Reynolds-number independence for the lift coefficient. They also display similarity in the lift-coefficient history; namely rapid initial growth that plateaus prior to a secondary rise. However, the experimental results diverge slightly from the predictions: the onset of the initial rise in measured lift occurs earlier and rises to a higher level than is predicted.

Introduction

Flapping flight is of interest to aerodynamicists and airframe designers because of its potential to enable efficient and highly manoeuvrable flight with 'micro' air vehicles (MAVs). The means used by natural flyers to generate lift with flapping wings in excess of that expected from classical aerodynamics has been the topic of much research, but understanding remains incomplete. In the work described in this and a related paper [1], fundamental aspects of flapping flight are examined through experimental and numerical investigations of the unsteady lift-generation mechanisms exploited by natural flyers.

During 'normal hovering' [15], exhibited by many insects as well as hummingbirds, each wing performs a horizontal sweeping motion at a relatively constant, high angle of attack. The wing flips at the stoke extremes, so that the same edge leads on both the morphological down- and up-strokes. The kinematics of normal hovering can be decomposed into largely discrete elements: a sweeping motion starting from rest at a constant angle of attack and a rotation about the span of the wing (a pitch reversal) at the end of each half-stroke [15]. Isolating the aerodynamic effects created by these unsteady motions enables a deeper understanding of the lift-generation mechanisms of flapping flight [14].

In the current work, the lift on a rigid, rectangular plate is measured as the plate rotates from rest to a steady angular velocity. The wing has a chord of c and a length, l, equal to c, yielding an aspect ratio (l/c) of one. Its thickness is equal to 4.5% of the chord length. The wing rotates about an axis located $0.52c$ from its root. The Reynolds number, Re, is given by

$$Re = \frac{U_{r_g} r_g}{\nu} , \qquad (1)$$

where r_g is the radius of gyration of the wing (located at its mid-span), U_{r_g} is the tangential velocity at the radius of gyration during the steady part of the motion and ν is the kinematic viscosity of the fluid (here, room air, for which $\nu = 1.461 \times 10^{-5}$ m²/s). The tangential velocity at the radius of gyration during the steady part of the motion is given by

$$U_{r_g} = \Omega_0 r_g , \qquad (2)$$

where Ω_0 is the angular velocity of the wing during the steady motion (its maximum value). For these experiments, Re ranges from 7600 to 31 000; and the pitch angle of the wing with respect to the plane of rotation (its angle of attack) is 60°.

Previous work has been performed on this fundamental fluid-mechanics problem. Ozen and Rockwell [11] employed particle-imaging velocimetry to characterise the flow structure around the rotating wing and identified the formation of a coherent, stable leading-edge vortex (LEV); while Garmann, Visbal, and Orkwis [6] used a computational fluid dynamics (CFD) technique to simulate the flow and predicted the unsteady lift and drag histories. Further experimental investigation is warranted to fully validate the CFD solution; and the current work provides a direct, quantitative comparison between the CFD results and measurements of the lift created by the unsteady motion of a rotating wing.

Methodology

Experimental Set-Up

The experiments were performed on the test rig illustrated in figure 1 [8]. It utilises two shafts capable of rotating a wing about perpendicular axes. Each shaft is supported by bearings and rotated by a low-inertia, brushless Parker SMB82 motor [12] at a ratio of 3:1 through a gearbox connecting the motor to the shaft. One of the shafts creates a flapping or sweeping motion, while the other is connected to a right-angle gearbox to provide a pitching motion. Because the experiment under discussion here utilised a constant angle of attack, the pitching axis was not employed.

A Nano17Ti load cell from ATI [2] was used to collect force and torque data for the wing on three orthogonal axes. The sensor was mounted rigidly to the shaft of the 'flapping axis' shown in
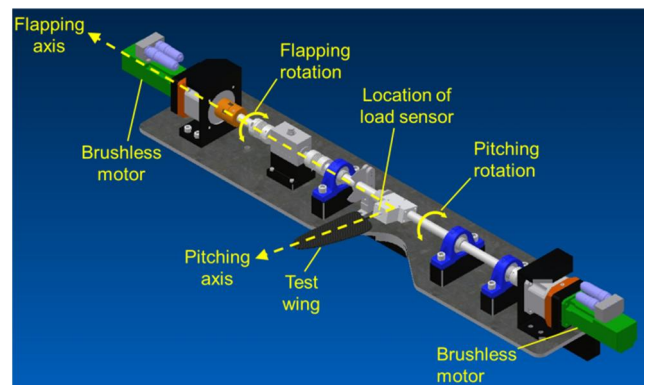

Figure 1. The arrangement of the flapping-wing test rig.

figure 1; and a collet was fixed to the top of the sensor to hold the test wing (in this case, a rigid, square plate). The sensor was oriented so that one of its axes lay parallel to the plane of rotation of the wing and another was perpendicular to it. Thus, the force measured on the second axis corresponded to the lift force.

The sensor output was split into six channels that were input to a Microstar analogue data-acquisition board (MSCB080) with a DAP5216a/627 processor [10], which sampled the voltages at 20 kHz with 16-bit resolution. The signals were then converted by the host computer into force and torque values [2]. The signals from a quadrature encoder mounted on the flapping shaft were recorded simultaneously to record the temporally resolved position of the wing.

The 110-mm × 110-mm test wing was constructed from 5-mm-thick Balsa-wood sheet and had half-rounded leading and trailing edges. The wooden frame of the wing had square cut-outs to reduce its mass and was supported by a stem made of carbon-fibre tubing, centred at the wing's mid-chord. Araldite glue was used to bind the stem to the frame. Sail repair tape was wrapped around the frame, covering the cut-outs and providing a smooth surface. A lightweight and rigid wing was desired, and the rigidity of the test wing was verified by use of a motion-capture system while it was subjected to the motion described below [13, 9].

Motion Specification

The motion implemented numerically by Garmann *et al.* was replicated experimentally to a very close approximation. The motion is essentially rotation at a constant angular velocity from an arbitrary starting angle, $\varphi = 0$, to the total angle swept by the wing, $\varphi = \varphi_0$. The motion occurs over an elapsed time that provides the angular velocity (Ω_0) corresponding to the desired Reynolds number for a particular experiment [eqs. (1) and (2)]. Time, t, is non-dimensionalised by the convective flow time (c/U_{r_g}):

$$\tau = t U_{r_g} / c , \qquad (3)$$

By definition, the motion starts at τ_1 and ends at τ_2, where

$$\tau_2 = \tau_1 + \varphi_0 / \Omega_0^* . \qquad (4)$$

The angular velocity has been normalised by the number of chord lengths travelled per unit time at the translational speed of the radius of gyration (U_{r_g}/c):

$$\Omega_0^* = \Omega_0 c / U_{r_g} \left(= c / r_g \right). \qquad (5)$$

This unsmoothed motion may be expressed as

$$\varphi(\tau) = \begin{cases} 0, \text{for } 0 \le \tau \le \tau_1 \\ \Omega_0^* \tau, \text{for } \tau_1 < \tau \le \tau_2 \\ \varphi_0, \text{for } \tau_2 < \tau \end{cases} \qquad (6)$$

and is illustrated in figure 2.

To avoid sharp accelerations, Garmann *et al.* implemented a smoothed version of the piecewise motion profile, described by a continuously differentiable function [4]:

$$\varphi(\tau) = \frac{\Omega_0^*}{2a} \ln\left[\frac{\cosh(a(\tau - \tau_1))}{\cosh(a(\tau - \tau_2))} \right] + \frac{1}{2}\varphi_0 , \qquad (7)$$

where the definitions of τ, φ_0, and Ω_0^* are as given previously. As shown by figure 2, where the motion profile described by equation (7) is plotted, this function provides rotational motion at a relatively constant velocity between τ_1 and τ_2, where τ_1 is an input parameter and τ_2 is again given by equation (4).

Consistency with the CFD analysis was maintained in the experiments by setting τ_1 and the smoothing parameter, *a*, equal to 2 and 2.6, respectively, which are the values used by Garmann *et al.* Because Ω_0^* is governed purely by the geometry of the wing [eq. (5)] and the geometry used experimentally was identical to
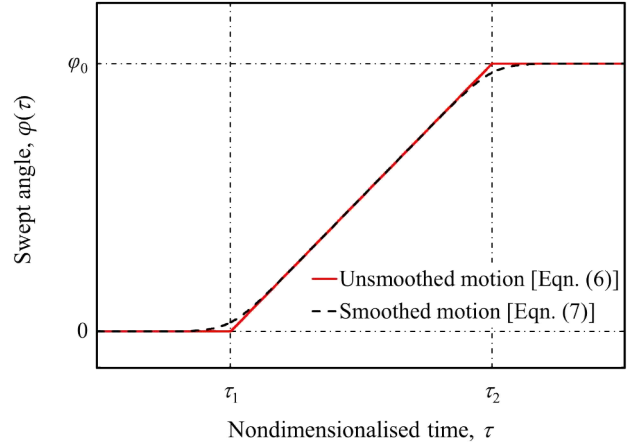

Figure 2. Wing motion used in CFD simulations by Garmann *et al.* [6].

that in the computations ($c/r_g = 0.98$), the values of Ω_0^* were the same.

Whereas Garmann *et al.* conducted CFD simulations in which the total swept angle (φ_0) was 2π (360°), the test rig on which the experiments were performed has an optical limit switch that keeps the test wing from coming into contact with the rig's support stand (Fig. 1) and dictated a maximum rotational angle of ~250°. To match the motion profile used in the computations as closely as possible and to make the temporal extent of the comparison as great as possible, the motion described by equation (7) with $\varphi_0 = 2\pi$ was used up to the mid-point of the motion [$\tau = (\tau_1 + \tau_2)/2 \approx 5.2$ and $\varphi = \pi$]. Beyond that point, the wing was decelerated smoothly and rapidly to avoid damage to the wing or sensor that could occur if contact were made with the support stand. The deceleration was significantly more rapid than that described by equation (7); however, the motion used in the experiments closely matched that of the CFD simulations for the first 180° of motion. The simulations indicate that this period encompasses the development of lift on the wing [6], thus the primary goal of the motion-control strategy was reached.

The desired motion was produced by a brushless motor [12] and a Galil DMC-4060 motor controller, using the latter's 'position–velocity–time' (PVT) function [5]. To generate a continuous motion, the desired profile is discretised and provided to the controller as a series of relative displacements and velocities, along with time intervals between the points. The PVT function interpolates between the points using 3rd-order polynomials. The PVT mode produces a smooth rotational motion, avoiding sharp accelerations caused by discontinuities in the programmed profile.

The tests were performed with values of maximum angular velocity (Ω_0) corresponding to Reynolds numbers of 7600, 10 000, 15 000, 21 000, and 31 000 [eqs. (1) and (2)]. Because in some instances, a programmed PVT profile resulted in significant inaccuracies in the motion produced by the motor, a process of trial and error was used to determine the optimal number of PVT points for each test condition. Motion profiles obtained in a single run at each condition are shown in figure 3, along with the profile used by Garmann *et al.* (the desired motion). The angle at which the limit switch would stop the motion (were it reached) is also indicated. As can be seen, a close match to the desired motion was obtained up to $\varphi \approx \pi$ (180°) in each case; however, small differences in the motion profiles are observable in figure 3 during this phase of the motion.

The significant departures from the programmed motion seen after the wing reached 180° are due to the fact that the motor decelerated slightly differently in each run. However, as only the initial period of the motion, during which lift increases, was of interest, the differences in deceleration were unimportant.
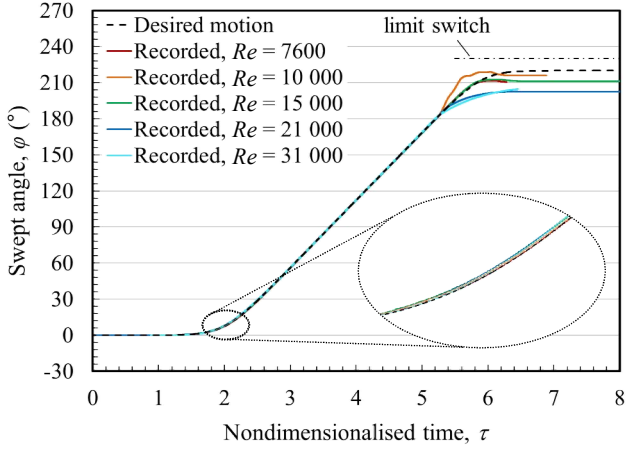
Figure 3. Phased-averaged motion of the test wing for runs at different Reynolds numbers, compared with the desired wing motion.

Data Post-Processing

Several post-processing routines were used to extract the desired quantities from the raw data recorded during the experiments. The force and torque values output by the Nano17Ti sensor were filtered with a 2nd-order low-pass Butterworth filter with a cut-off frequency of 25 Hz. Filtering was necessary because of mechanical vibrations in the rig that were recorded as high-frequency noise in the signals from the sensor. It was observed that when power was supplied to the motors, they generated vibrations even when stationary. These vibrations were not observed when the power supply was disconnected. Because the aerodynamics of the wing were unlikely to have produced such high frequencies in the measured forces and torques [6], it was improbable that low-pass filtering would eliminate aerodynamics-related characteristics.

The signals output by the encoder on the flapping axis during each run were converted into a corresponding angular-position profile. The angular velocity during the steady portion of the motion was evaluated by least-squares fitting the data recorded between $\varphi = 60°$ and $120°$. The computed angular velocity was used to non-dimensionalise the accompanying temporal data [eq. (3)] and to evaluate the actual Reynolds number achieved during the test [eqs. (1) and (2)]. The dimensionless time (τ) was also shifted to create a common temporal axis with the CFD data by use of the angular-position data for each run.

The data recorded in each force or torque channel during 20 individual runs at a given test condition were phase averaged to reduce any residual error. Finally, the phase-averaged lift force, L, was converted into a coefficient of lift, C_L, using the definition:

$$C_L = \frac{L}{\frac{1}{2}\rho U_{r_g}^2 S} , \qquad (8)$$

where ρ is the density of the air (1.225 kg/m³ for dry air at 15 °C and 1 atm) and S is the planform area of the wing [7].

ATI, the sensor manufacturer, guarantees that the relevant force channel has a random error of no greater than ±1% of its full-scale range of 8 N at the 95% confidence level [2]. The calibration report, however, states that the standard deviation of the random error for loading cases similar to that in the current experiments is (on average) ±0.05% of the full-scale range or ±0.004 N. Because the results here are averages of 20 individual measurements, this value is divided by √20 to yield an estimated standard error in the measured lift force of ±0.001 N [3]. This uncertainty can be used to estimate the error in the measured lift coefficient. The lift force increases with the square of the steady translational velocity of the wing [for a constant lift coefficient, eq. (8)], whereas the Reynolds number is proportional to its velocity [eq. (2)]. Thus, the uncertainty in the measurement of lift

coefficient is inversely proportional to Re^2. The standard error in the lift coefficient measured at $Re = 7600$ is ±0.12; whereas for $Re = 31\,000$, the error is estimated to be ±0.0072.

Results

Figure 4(a) provides a comparison of the measured lift-coefficient history at each test condition with CFD predictions by Garmann *et al*. While the experiments were conducted for Reynolds numbers from 7600 to 31 000, CFD results are available for Reynolds numbers of 7200 to 60 000 [6]. These differences are unimportant, however, as both the experimental and computational datasets indicate that the lift coefficient is (at most) weakly dependent on Re in this range.

A two-stage process of lift development is observed in the CFD results and in the experimental data for each Reynolds number (with the possible exception of $Re = 31\,000$); however, there are some marked differences between the two datasets. The measured lift coefficient in each case rises smoothly from zero at $\tau \approx 1$ to a plateau that begins at $\tau \approx 2$, just as the wing reaches its maximum angular acceleration [given by the second differential of $\varphi(\tau)$, eq. (7)]. The CFD results show a similar initial rise; however, the plateau occurs later and is lower (at $C_L \approx 1.3$) than that observed experimentally ($C_L \approx 1.45$, on average).

Small differences in the slope of the measured lift-coefficient histories in figure 4(a) at $1 < \tau < 2$ are likely the result of random error in the force measurements and inaccuracies in the motion profiles. Based on the fact that the recorded lift coefficient begins to rise at $\tau \approx 1$, when the wing motion is barely measureable, it is evident that small variations can generate observable changes
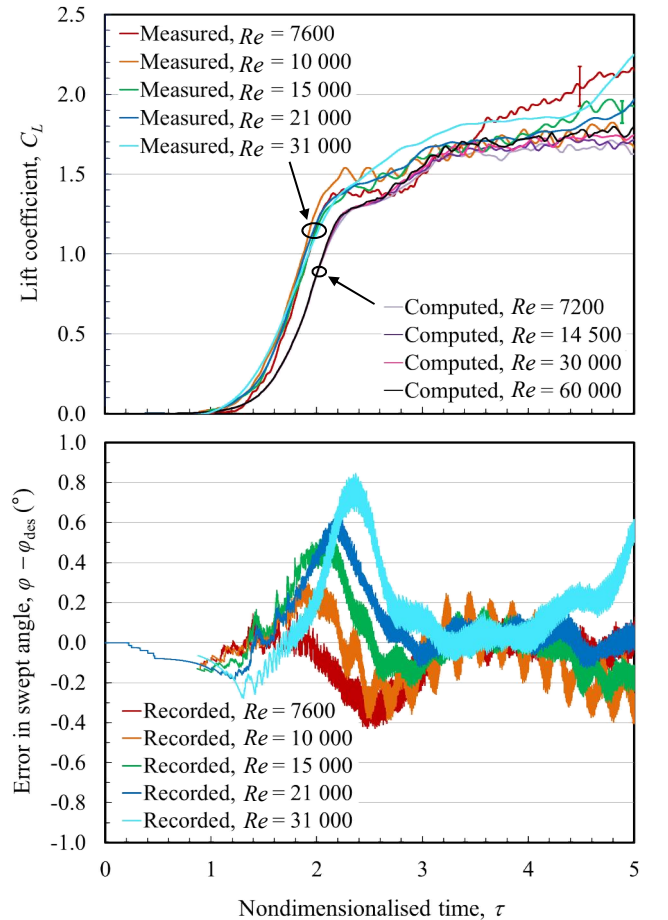

Figure 4. (a) Lift-coefficient history at different Reynolds numbers, measured in the current work and numerically predicted by Garmann *et al*. [6]. (b) Error in the angular position of the wing with respect to the desired motion described by equation (7).

in lift coefficient. The expanded portion of the motion profiles displayed in figure 3 at $\tau \approx 2$ shows very tiny differences amongst the profiles; nonetheless, even these may be detectable.

The estimated standard errors in the experimental data are shown in figure 4(a) by the error bars on the lift-coefficient measurements at Reynolds numbers of 7600 and 15 000. They illustrate that the uncertainty decreases with increasing Reynolds number and further explain the differences in the measured lift-coefficient histories at different test conditions.

Both sources of error in the measurements are deemed inconsequential when the whole experimental dataset is evaluated during the period of rapid lift growth ($1 < \tau < 2$). The difference between the grouped experimental results and the cluster of CFD results, which show *Re*-independence in this phase of the motion, is unlikely to be attributable to errors in the measurements. One other possible source of discrepancy is the difference in the leading- and trailing-edge geometries of the wings: the wing used in the experiments had rounded leading- and trailing-edges, while the CFD analysis considered a wing with squared edges [6].

After the initial plateau in lift, the CFD results show a secondary rise and subsequent gradual increase in lift force (at $\tau > 3$) because of the continued growth of the LEV and root vortex [6]. The experimental results show a similar secondary increase in lift coefficient, though it appears to start slightly later. The trend in the experimental data is less clear for $\tau > 3$ because the experimental data obtained at different test conditions diverge, with some measurements showing an increase in lift (*Re* = 7600 and 31 000) and others remaining at a constant level (*Re* = 10 000).

These differences were likely caused by variations in the motion profiles. The difference between the recorded and desired profiles [$\varphi(\tau)$ and $\varphi_{\mathrm{des}}(\tau)$, respectively] is illustrated for each test case in figure 4(b). The correlation between the lift-coefficient histories and the errors in the motion profiles is clear, particularly for $\tau > 4$. Oscillations observable in the motion recorded for *Re* = 10 000 and 15 000 explain the periodic variations in the corresponding lift-coefficient histories. The findings highlight a need to achieve accurate motion control.

Conclusion

The experimental results presented here provide quantitative validation of published computational predictions for a canonical test case of a wing rotating from rest in a quiescent fluid. Previous experimental studies relying on flow-velocimetry techniques served to partially validate the simulation; however, such methods do not provide accurate integrated aerodynamic parameters (lift and drag forces or pitching moment). In contrast, the experimental approach described here enables detailed lift-force histories to be compared with the same integrated quantity from the CFD analysis. It is thus an attractive complement to flow-imaging techniques and can add significant confidence to the predictive capability of the CFD analysis.

The Reynolds-number independence found in the CFD results for chord-based Reynolds numbers in the range tested (7600 to 31 000) was confirmed for lift-coefficient histories obtained experimentally; however, a significant difference was observed in the initial increase in lift at the start of the wing motion. The discrepancy is unlikely to have resulted from experimental error, though differences in the geometries of the leading- and trailing-edges of the wings used experimentally and computationally merit further investigation.

Non-negligible uncertainty remains in the experimental data obtained after the vortical flow field around the wing was established and a plateau in the lift coefficient was reached, however, because of small deviations in the motion profiles from that used in the CFD analysis. Further refinements of the testing procedure may address these deficits, and the coefficients of drag and pitching moment may be extracted from experimental data in future work for direct comparison with the CFD results.

References

[1] Agon, A., M. Giacobello & J.L. Palmer, Flow Structures on a Low-Aspect-Ratio Wing Undergoing a Pitch–Ramp–Hold Manoeuver in a Uniform Cross-Flow, in *19th Australas. Fl. Mech. Conf.*, 2014.

[2] ATI Industrial Automation, Inc., *F/T Data Acquisition (DAQ) Six-Axis Force/Torque Sensor System, Compilation of Manuals, Manual # 9610-05-1017 DAQ.* January 2010. Available from: www.ati-ia.com/zh-CN/app_content/documents/9610-05-1017%20DAQ.pdf [cited 22 January 2013].

[3] Devore, J.L., *Probability and Statistics for Engineering and the Sciences.* Monterey, CA, USA, Brooks/Cole Publishing Company, 1982.

[4] Eldredge, J.D., C. Wang & M.V. Ol, A Computational Study of a Canonical Pitch-up, Pitch-Down Wing Maneuver. Paper AIAA-2009-3687 in *39th AIAA Fl. Dyn. Conf.*, New York, NY, USA, American Institute of Aeronautics and Astronautics, Inc., 2009.

[5] Galil Motion Control, Inc., *DMC-40×0 Series, Ethernet/ RS232 Accelera Series, 1–8 Axes*, 2014. Available from: www.galilmc.com/catalog/cat40x0.pdf [cited 15 July 2014].

[6] Garmann, D.J., M.R. Visbal & P.D. Orkwis, Three-Dimensional Flow Structure and Aerodynamic Loading on a Revolving Wing. *Phys. Fl.*, **25**, 2013.

[7] Hale, F.J., *Introduction to Aircraft Performance, Selection, and Design.* New York, John Wiley & Sons, Inc., 1984.

[8] Jones, M.B., A. Valiyff & J.R. Harvey, Dynamic Analysis of a Flapping-Wing Test-Stand in *14th Aus. Int'nal Aerosp. Cong.*, Mascot, NSW, Australia, Royal Aeronautical Society (Australian Division) and Engineers Australia, 2011, pp. 372–382.

[9] Jones, M.B., A. Valiyff & J.R. Harvey, Flexibility of an Ornithopter Wing Tested in a Wind Tunnel, in *28th Int'nal Cong. Aeron. Sci.*, **2**, editor I. Grant, Red Hook, NY, USA, Curran Associates, Inc., 2012, pp. 855–861.

[10] Microstar Laboratories, Inc., *Filtered Analog Input Expansion: MSXB 048*, 2013. Available from: www.mstarlabs.com/access/xb048.html [cited 9 July 2014].

[11] Ozen, C.A., and D. Rockwell, Three-Dimensional Vortex Structure on a Rotating Wing. *J. Fl. Mech.*, **707**, 2012, 541–550.

[12] Parker, *SMB/SMH Series, Low Inertia Servo Motors*, November 2013. Available from: www.galilmc.com/index.php [cited 15 July 2014].

[13] Vicon Motion Systems, Ltd., *T-Series*, 2014. Available from: www.vicon.com/System/TSeries [cited 25 June 2014].

[14] Wang, Z.J., Dissecting Insect Flight. *Ann. Rev. Fl. Mech.*, **37**, 2005, 183–210.

[15] Weis-Fogh, T., Quick Estimates of Flight Fitness in Hovering Animals, Including Novel Mechanisms for Lift Production. *J. Exp. Biol.*, **59**, 1973, 169–230.